Proceedings of the ASME 2023
International Mechanical Engineering Congress and Exposition
IMECE2023
October 29-November 2, 2023, New Orleans, Louisiana

IMECE2023-113065

DESIGN OPTIMIZATION OF ADDITIVELY MANUFACTURED COMPONENTS USING SIMULATION-BASED ANALYSIS OF INFILL STRUCTURES

Karim Asami[1,2], Sebastian Roth[1,2], Michel Krukenberg[1], Claus Emmelmann[1,2]

[1]Technical University Hamburg (TUHH), Hamburg, Germany
[2]iLAS – Institute of Laser and System Technologies, TUHH, Hamburg, Germany

ABSTRACT

Additive manufacturing (AM) has revolutionized the manufacturing industry, allowing the production of complex, lightweight components with specific properties. This has created opportunities for customized parts with optimized performance and cost-efficiency compared to traditional manufacturing.

Infill structures are used to fill the voids inside the component during layer-by-layer manufacturing. These structures, such as grids and honeycombs, optimize mechanical properties, reduce weight, and save production time. However, investigating the mechanical properties of components with different infill structures is typically done experimentally, which is time-consuming and expensive.

This paper proposes a simulation-based approach to investigate the influence of infill structure parameters on the mechanical properties of components made from AISI 316L stainless steel. Two-dimensional grid and honeycomb infill structures are studied, considering infill degree, cell wall thickness and spatial orientation relative to the load direction. The study employs a parametric design approach to generate different infill structures for simulation and validation.

This paper provides a simulation-based methodology for varying and evaluating design parameters for AM processes using grid and honeycomb infill structures. The findings can be used to optimize lightweight component design for specific applications, improving performance and cost-efficiency. The study contributes to the field of Design for Additive Manufacturing (DfAM).

Keywords: Design Analysis, Simulation, Infill, Grid, Honeycomb, 316L, MEX/M, L-PBF, Additive Manufacturing, DfAM

1. INTRODUCTION

Additive Manufacturing (AM), also known as 3D printing, is a revolutionary manufacturing process that has gained significant attention in recent years. Unlike traditional subtractive manufacturing methods, AM builds three-dimensional objects layer-by-layer, allowing for unprecedented design freedom and versatility. With its ability to create complex geometries and functional structures, AM has found applications in various industries, including aerospace, automotive, medical, and consumer products, among others.

The field of AM has evolved rapidly, with advancements in materials, processes, and equipment, leading to improved capabilities and expanding the possibilities of manufacturing. From polymer-based systems to metal and ceramic AM, the technology has opened new paths for producing parts with enhanced mechanical, thermal, and electrical properties. Moreover, the ability to fabricate customized parts with no limitations in the design process has enabled lightweight optimized designs and reduced the material consumption making AM an increasingly attractive option for modern manufacturing.

One approach to generate weight optimized designs is through computer aided topology optimization, where a component is iteratively analyzed for stress distribution and its shape is modified to save material and space. However, this process is computationally intensive and time-consuming, and it results in changes to the external shape of the components, which is not intended in some cases. [1, 2]

Another method is to perform structural optimization by incorporating infill structures in additively manufactured components. Infill structures can be made out of lattice structures, built up in the internal cavities of a component, ideally tailored to the specific load requirements of the component. This approach offers the potential to achieve weight savings without altering the external shape of the components.

Lattice structures are known for their high strength-to-weight ratio. They are typically composed of repeating unit cells

with open spaces or voids, which reduces their overall weight while maintaining structural integrity. This makes them ideal for applications where weight reduction is critical, such as aerospace, automotive, and transportation industries. Lattice structures therefore use materials efficiently by optimizing the distribution in the structure regarding the load requirements of the part. [3, 4]

Additionally, lattice structures are highly customizable. The geometry parameters, such as orientation angle, wall thickness and overall filler content can be altered to meet the specific design requirements. This makes them versatile for a wide range of applications and allows the optimization of the infill structure for different use cases. [5] The inner structure of turbine blades for example can be filled with lattice structures. The flow optimized outer shape of the blade remains untouched, while the overall weight is reduced significantly even though the load requirements are still fulfilled.

However, most infill structures are highly anisotropic. [6] Therefore, the exact knowledge of the load capacity in different angles of the lattice structure is required to fulfill the design requirements of the part. In this paper, the focus is on rather simple infill structures, based on honeycombs and grid structures. Those can be manufactured faster in the e.g. the Material extrusion of metals (MEX/M) process due to size, instead of generating more complicated infills structures with e.g. gyroid-cells. [7,8,9] Therefore, this approach can be applied to many already existing use cases without the need of new development cycles.

To solve such a problem, this paper aims to provide a methodology based on simulated infill structures to choose the optimal parameters for a specific lattice structure on a given part with known load requirements. Additionally, angle-dependent properties where infill structures can be altered to tackle dynamic loads or alternating load directions are provided.

2. MATERIALS AND METHODS

2.1 Testing methods

The following testing methods for investigating the load behavior were used: Compression test according to ASTM E9 [10] and 3-point bending test according to ISO 7438 [11].

The compression test according to ASTM E9 is a standardized testing method used to investigate the load behavior of material samples under compression. In this test, a sample is loaded in a testing machine until it fails, refer to [10]. This method allows conclusions to be drawn about important material parameters such as the modulus of elasticity, which describes the stiffness of the material, and the tensile strength, which indicates the maximum load-carrying capacity of the material. The compression test is particularly relevant when components in later application are subjected to combined bending and compressive loads.

The 3-point bending test according to ISO 7438 is another common testing method used to investigate the load behavior of material samples under bending loads. In this test, a sample is supported on two rollers and loaded in the middle until it fails, refer to [11]. This method also allows conclusions to be drawn about material parameters such as the E-modulus and tensile strength. The 3-point bending test is particularly relevant when components in later application are subjected to bending loads, which often act in combination with compressive loads on the component.

In practice, the compression test and the 3-point bending test are commonly used to characterize the load behavior of materials and ensure meeting the requirements of the intended application.

The investigation of the load behavior of infill structures is based on these two testing methods. The two loading conditions are simulated and used for localizing the most heavily loaded areas within the samples and for examining the influences of the parameters of different infill structures. Static test loads are used instead of dynamic loading until sample failure for the investigation of stress distribution within the samples.

2.2 Variation of Infill Structure

In this section, the variation and consequently the parameterization of the infill structures are presented. The starting point of the variations is a solid specimen (φ = 100 %), which is simulated under compression and 3-point bending. The infill structures are investigated in separate series of tests limited to the degree of infill, the cell wall thickness, and the orientation of the infill relative to the load in order to be able to consider the influence of the individual parameters in isolation. The external dimensions of the specimens correspond to the dimensions of the reference specimens of the test setups: the cylinders have the diameter d = 40 mm and height L = 40 mm, the beams have a length of L = 80mm and a height/width of a = 20 mm (see fig. 2).

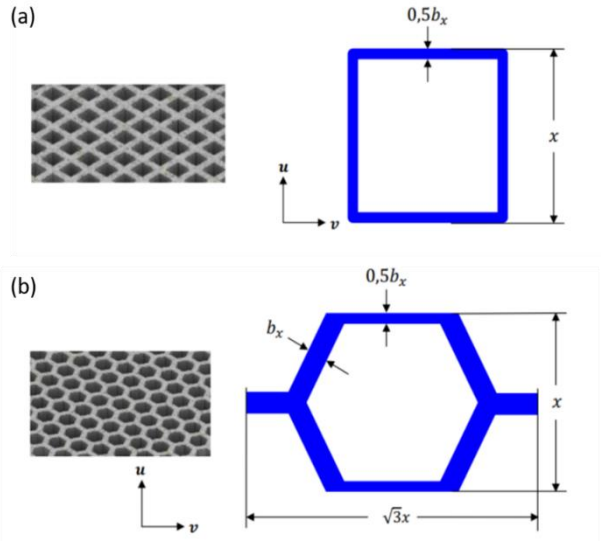

FIGURE 1: Parametrization of the infill structure; (a) parametrization of the grid structure; (b) parametrization of the honeycomb structure.

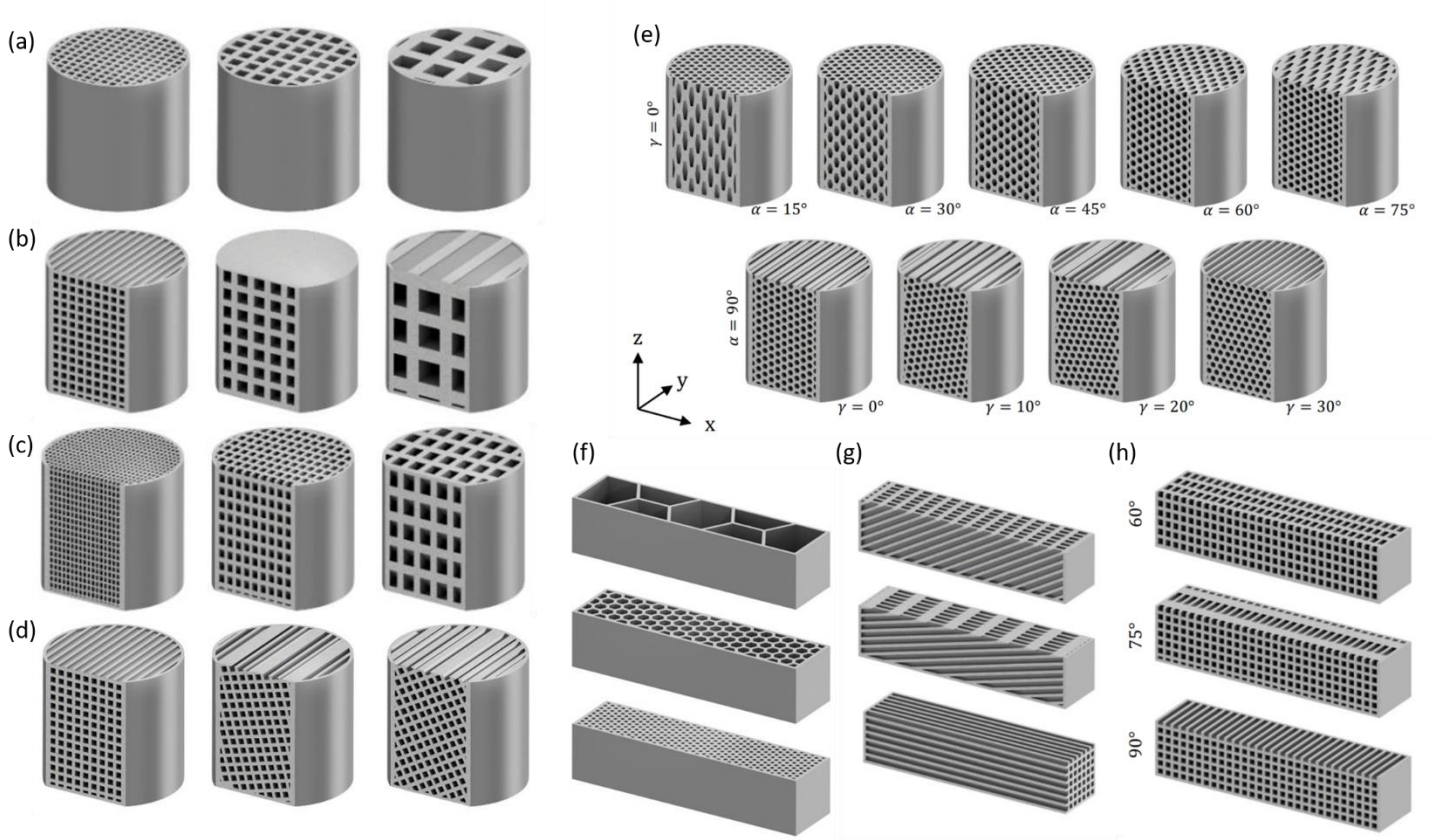

FIGURE 3: Variation of the infill structure; (a)-(e) Variation of the infill structures used in the compression test: Variation of the orientation and angle, variation of the wall thickness, variation of the infill type (grid and honeycomb); (f)-(g) Variation of the infill structures used in the 3-point bending test: variation of the orientation, angle, wall thickness and infill type.

For the parametrization of the infill structures the specimen have to be separated into identical cells that represent the wall of the infill structure as well as the pores. The base area of each of these cells is composed of the proportion of cell wall thickness and pore size. The ratio of the cross-sectional area filled with material to the pore volume represents the infill degree and can be calculated for each cell by equations 1.1 for the grid-based infill structure and with equation 1.2 for the honeycomb infill structure. The wall thickness b_x is varied between 0.5 mm and 10 mm.

$$\varphi_{grid} = \frac{A_{grid} - A_{pore}}{A_{grid}} = \frac{x^2 - (x - b_x)^2}{x^2} \qquad 1.1$$

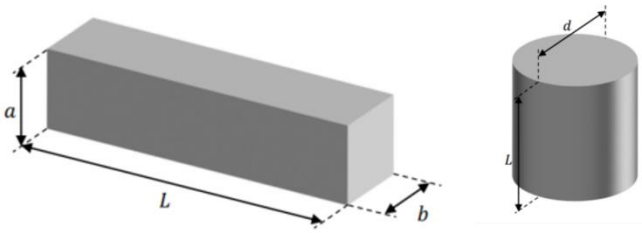

FIGURE 2: Representation of the specimen dimensions.

$$\varphi_{grid} = \frac{A_{hc} - A_{pore}}{A_{hc}} = \frac{\sqrt{3} \cdot x^2 - \sqrt{3} \cdot (x - b_x)^2}{\sqrt{3} \cdot x^2} \qquad 1.2$$

The variation of the infill structure is done in *Autodesk Inventor* by a parametrization of the infill structure according to figure 1. Additionally, the infill structures were oriented horizontally or vertically in the specimens. To tilt the infills, three angle-dependencies were introduced: α rotates the infill structure around the x-axis, β around the y-axis while γ rotates the structure around its longitudinal axis, refer to figure 3 (c)-(e) and (g)-(h). The angles of the compression specimens are varied between α = [0°,15°,…,75°,90°] and γ = [0°,10°,…,30°]. β is not varied separately due to the rotational symmetry of the compression specimens. Because the 3-point bending specimen do not have the same rotational symmetry, more specimen had to be simulated in order to achieve the same angle variations. They were varied between α = [0°,15°,…,75°,90°], β = [0°,15°,…,75°,90°] and γ = [0°,15°,…,45°], which is varied depending on the selected structure with the corresponding angles.

2.3 Simulation setup

In this section the setup of the simulations is presented. The simulation was performed with the FEM software *Altair Hyperworks 2021. Hyperworks* provides the benefit, that loads can be directly applied to the infill structure, rather than be absorbed by the shell of the part. A comparison between the

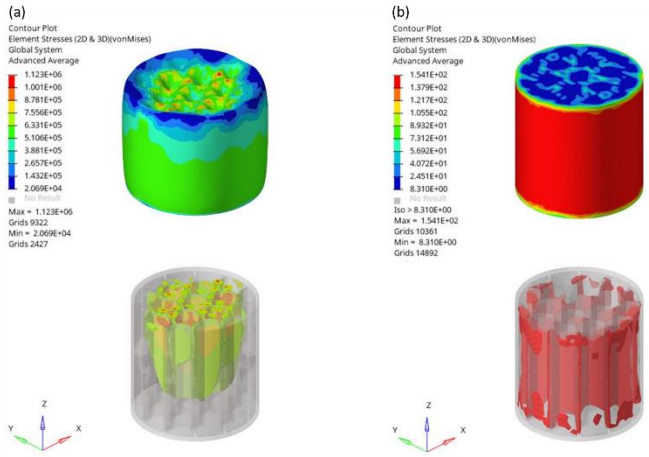

FIGURE 4: Differences in the simulation of the stress distribution with different softwares: (a) Simulation performed with Inventor; (b) Simulation performed with Hyperworks.

results of a simulation that was performed with *Inventor 2022* and a simulation performed with *Hyperworks* is presented in figure 4. The upper pictures are showing the deformed shape of the specimen; the bottom pictures are showing the stress distribution in the infill structure. As one can clearly see, the direct introduction of the load into the shell leads to an incorrect simulation of the loads in the infill structure. This can be neglected by the selection of an ideal rigid connection in Hyperworks and leads to the correct load of the infill structure.

The element size of the used mesh is set to 2 mm and the minimum element size is set to 0.1 mm. Local refinement of the meshing using Proximity and curvature is omitted, because the focus is not on the exact resolution of the stress peaks in small areas of the geometry. The FE model of the cylindrical specimens is constructed from tetra-elements with four nodes each which are well suited for the approximation of complex three-dimensional structures.

For the bending beam, the 3D type of the elements is set to mixed and the 2D type is set to quads. Due to the square bases of the pyramid-shaped elements, an even distribution of the nodes on the specimen surface is achieved, which can be used for the approximation of the support rollers and the compression die. Depending on the internal geometry tetrahedra or pyramids are used to best represent the specimen surface.

To validate the generated mesh, a convergence study was performed. The mesh was implemented for all simulated specimens, regardless of individual size of the analyzed infill structure. 84 cylindrical compression specimen and 96 3-point-bending specimen were simulated.

The simulation is build according to the testing methods presented in section 2.1. In the compression test setup, the mounting of the specimen allows an increase of the contact area between the specimen and the testing machine under the assumption of an ideal frictionless contact. As a result, the stress concentrations in the edge areas of the cylindrical specimen's end faces and bulging of the lateral surface are reduced to maintain the focus on the stresses inside the infill structure. This support is applied to the entire face of the compression specimen.

For the support of a 3-point bending specimen, two support rollers are used [10] to ensure rolling of the beam and prevent an incorrectly high tensile stress at the bottom side of the beam during the bending test. Accordingly, the support is only associated with the specimen surface in the area of these support rollers. The spacing of the support rollers is l=70 mm.

The test load for the compression test according to [9] is set to F_D=50 kN, the test series with grid-shaped infill structure and a variable infill degree is additionally carried out with the loads F_D=100 kN and F_D=200 kN, to verify the assumed linear relationship between test load and simulated stress. A load of F_B=20 kN is chosen for the 3-point bending test simulation, since the stress level of this type of load is higher than that of a pure compression load.

The load analysis is evaluated qualitatively to show differences in stress between configurations. Therefore, the value of the test forces is secondary as long as it is constant across the series of tests to be compared and a linear elastic model is used.

As material, stainless steel 316L was chosen. The material properties that were used in the simulations are presented in table 1.

Table 1: Material properties used for the simulation.

Young's modulus	200 GPa
Poisson's ratio	0,27
Density	7,9 g/cm³

3. RESULTS AND DISCUSSION

The results of FEA strongly depend on the mesh setting. A trade-off between a fine resolution mesh and a reasonable computational effort has to be found in order to obtain reasonable results in an efficient way. Under a load longitudinal to the infill structure, no change of the simulated stress using different mesh sizes occur and does not allow any statement about the quality of the approximation. Under a load transverse to the infill structure, a relationship between stress and finite element size could be identified.

3.1 Compression simulation with the cylindrical shapes

The compression simulation has been performed with cylindrical specimens with grid and honeycomb as infill structures.
Figure 5 shows the maximum stress occurring as a function of the infill degree for cylindrical honeycombs and grid structures with the same wall thickness of 1mm at a compressive force of 50kN. As expected, the maximum stress decreases with increasing infill degree. This is in line with results from different research groups [8, 12] and also confirms the assumption that a higher material volume fraction of infill reduces local and global stress peaks by increasing the area of the absorbing force. The volume fraction of infill has a clear influence on the maximum stresses occurring in the component. For example, with an infill of 10% the maximum stresses are about 215MPa for grid

structures and 220MPa for honeycomb structures. In comparison, the stresses with an infill of 30% for grid and honeycomb structures are about 111MPa. This is a reduction in stress of 48% for grid and 30.8% for honeycomb structures. In comparison, the maximum stress in the infill reduces between 60% to 70% from 64.6MPa to 55.6MPa (14%) for the grid and from 63.5MPa to 55.7MPa (12%) for the honeycomb structures. Above 70% infill, the maximum stress is reduced by less than 10% regardless of whether grid or honeycomb structures are applied. Furthermore, in figure 5 it can be observed that both honeycomb and grid structures exhibit similarly large maximum stresses at the same load perpendicular to the infill orientation, since the area filled with infill is of similar size, which is confirmed in other publications [12].

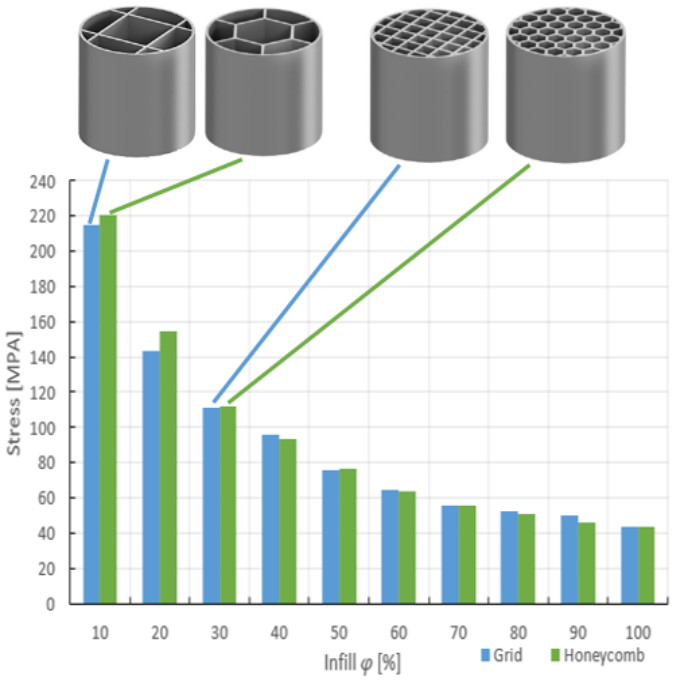

FIGURE 5: Representation of the maximum stress for different infill structures and percentages for cylindrical specimen geometries with a wall thickness of 1mm at a force of 50kN.

Table 2 displays the maximum stresses for grid structures at different infill for 100kN and 200kN force application. A linear relationship between the applied force and the stress can be observed. The stress at 100kN is always approximately half the stress at a force of 200kN, regardless of the infill percentage.

Table 2: Maximum stress depending of force and degree of infill for grid structures.

Infill [%]	Stress at 100kN [MPa]	Stress at 200kN [MPa]
10	415.37	839.52
20	285.69	571.77
30	221.96	445.18
40	179	356.8
50	151.96	304.11
60	126	252.3
70	113.1	226
80	99.56	200.8
90	88.68	177.2
100	87.11	159.6

Figure 6 illustrates the maximum stress as a function of the infill degree and infill orientation for 0° (perpendicular to the load) and 90° (transverse to the load). It is observed that for 90° infill orientation (transverse to the load), the maximum stress appearing also reduces with increasing infill. Furthermore, it can be recognized that at 20% infill the grid structures show a lower stress at 0° orientations with approx. 143 MPa than at 90° orientations with 205 MPa.

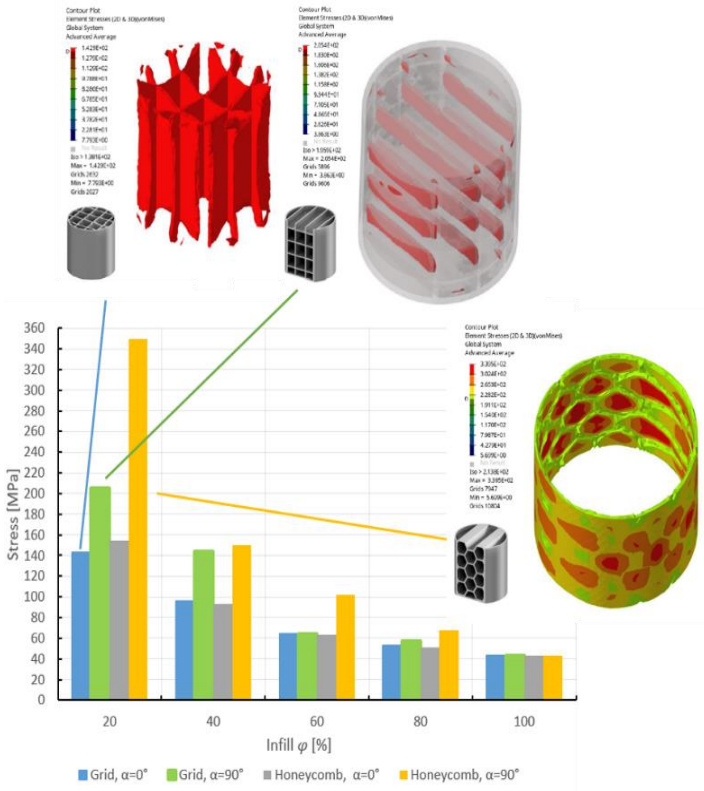

FIGURE 6: Illustration of the maximum stress for different infill structures for cylindrical specimen with a wall thickness 1mm at a force of 50kN at 0° and 90° infill orientation.

The illustrations of the simulations also display the maximum stresses appearing in the infill as well as in the shell structure. It should be mentioned that areas with lower stress levels have been filtered out to visualize more clearly the difference of the highly stressed and thus supporting parts of the specimen. In comparison, the maximum stress for honeycomb structures are higher with 154 MPa for the 0° orientation and approx. 350 MPa for the 90° orientation. In general, it can be observed that the 90°

oriented honeycomb structures have the highest maximum stresses for each percent infill. At 60% infill, the stresses in both orientations of the grid structures and the honeycomb structure at 0° orientations are approximately equal in magnitude of 62-64MPa. Only the honeycomb structure at 90° shows a high stress with approx. 100MPa. If the solid material (100% infill) is considered, the maximum stress is around 44MPa. The difference in the stress less than 25MPa can be observed for the three constellations (see fig. 6). Therefore, for further consideration the infill at 60% is identified as a threshold.

The following figure 7 illustrates the maximum stresses occurring at an infill of 60% with wall thickness of 1mm at different angular orientations α.

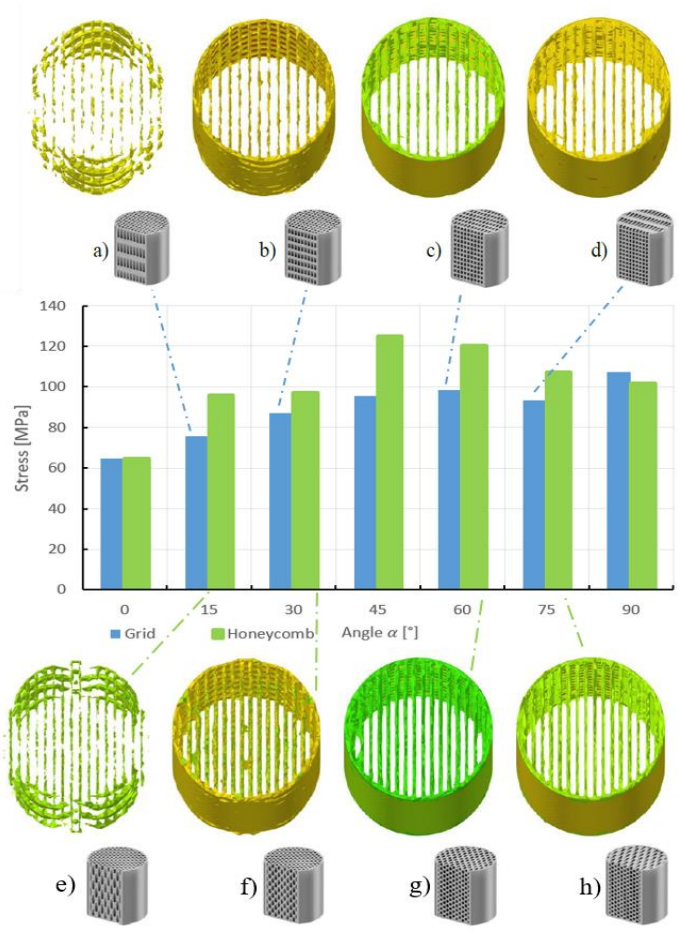

FIGURE 7: Representation of the maximum stress for 60% infill with grid (a-d) and honeycomb (e-h) structures for a wall thickness of 1mm at a force of 50kN for different angles α (the illustrations of the specimen stress distributions are filtered out to the same stress level).

The visualizations of the simulations show maximum stresses occurring in both the infill and the shell for all structures (see fig. 9 a-h). An increase of the stress can be recognized for both infill structures from 0° to 45° orientation from 64MPa to 96MPa (grid) and 125MPa (honeycomb). At 60° orientation, the highest stresses for grid structures occur at the 98MPa stress level. At 45° orientation, the highest stresses occur for honeycomb structures. At 90° orientation, the stresses are higher than at 0° orientation with approximately 102MPa (honeycomb) and 107MPa (grid). In this case, the stress of the honeycomb structures is one time lower than the stress of the grid structures for different angles α.

Varying the angle γ from 0° to 45° for 60% infill, 1mm wall thickness and a force of 50kN shows in the simulations that for the grid structures the maximum stress increases from 107MPa to 127MPa. This can be explained by the occurrence of shear stress in the grid structures due to a different load angle. Varying the angle gamma with the same boundary conditions show no increase in the maximum stress in the simulations for the honeycomb structures, which remain in the range of 97MPa to 102MPa. This is due to the rotational symmetry of the honeycomb, so that shear stress peaks can be avoided when varying the angle γ. Figure 8 shows the maximum stresses for the 0°, 45° and 90° infill orientations at 60% infill as a function of wall thickness. The simulated stress distribution is shown for the 90° orientation honeycomb structures, since the stresses are the highest (maximum 175MPa at 6mm wall thickness) with increasing wall thickness. It is visible that the maximum stresses in this orientation occur in the shell and at the edge structures of the infill. This observation can be explained by the parametric design approach, due to the increase in cell wall thickness allows fewer honeycomb cells to be generated, causing global stress peaks in these areas. Likewise, the stresses for honeycomb structures increase with increasing wall thickness for 45° orientations. The stresses for the 45° grid infill orientation are also increasing dependent to the wall thickness and is in the range from 95MPa to 131MPa. Wall thickness variation has almost no effect for the 0° orientation for honeycomb and grid structures. The stresses vary in these cases around 60MPa.

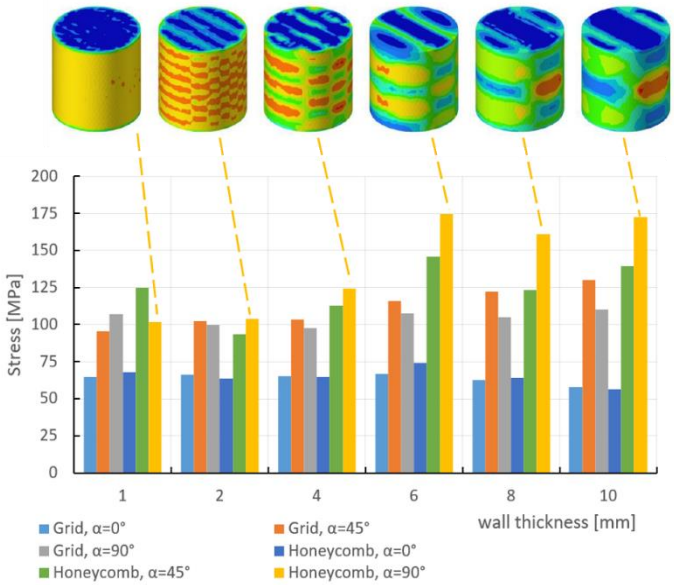

FIGURE 8: Stress distribution for 60% infill at a force of 50kN and 0°, 45° and 90° orientation for different wall thicknesses.

3.2 Bending simulation with beam elements

With the rectangular beams 3-point bending simulations were performed for different grid and honeycomb infill. Figure 9 shows the maximum stresses occurring as a function of the infill degree for rectangular beam elements with honeycombs and grid structures at the same wall thickness of 1mm and a load of 20kN. With increasing infill percentage, the maximum stresses decrease for honeycomb and grid structures. A comparable trend to the compression simulations can be observed, whereby the maximum stresses are consistently higher (see fig.5). Generally, for any percentage of infill, the maximum stresses for honeycomb structures are higher than for grid structures. It is evident that at 10% infill the maximum stress occurring with 1006MPa (grid) and 1121MPa (honeycomb) are significantly higher than the material-dependent tensile and compressive strength respectively of 485MPa [13] and result in component failure. Only above 60% infill the maximum stresses for honeycomb (466MPa) and for grid (400MPa) are below the maximum tensile strength of 316L, thus a threshold can also be identified in this case as well as for the compression simulations.

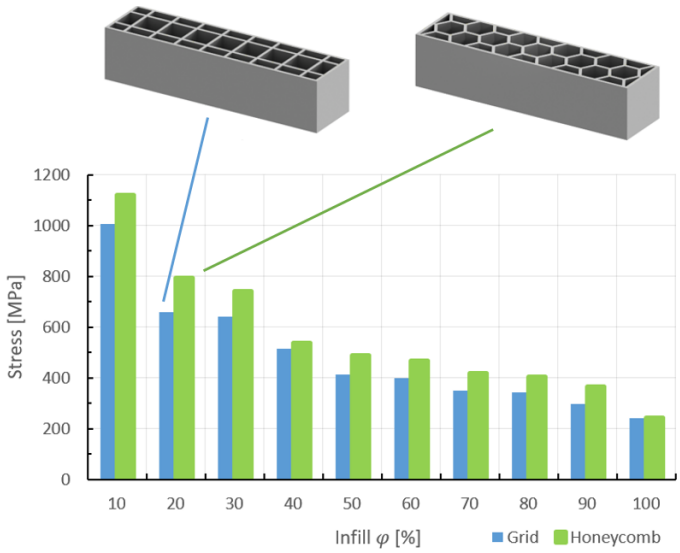

FIGURE 9: Representation of the maximum stress of different infill structures and percentages for rectangular beam specimen geometries with a wall thickness of 1mm and a load of 20kN.

The highest stresses occur in the area of 20kN force application in the specimen surface under the 3-point bending load for a wall thickness of 1mm (see fig. 10). Thus, the different orientations of the infill structures within the beam allow conclusions to be drawn about the stability of the loaded surface. At (α = 0°, β = 0°, γ = 0°) and (α = 0°, β = 90°, γ = 0°) the stress on the side walls is small and the transitions between the shell and the cell walls can be localized in the stress distribution on the shell. In addition, the tensile stress on the bottom of the beam under (α = 0°, β = 90°, γ = 0°) is lower than in the other two configurations, which have similar stress levels on the top and bottom of the specimen. This suggests a high stiffness of the infill structure under (α = 0°, β = 90°, γ = 0°) since the stress generated by the bending in the shell is lower than the stress due to the load application in the center on the top of the beam. The tensile stress on the bottom side in symmetrically designed bending specimens should theoretically be equal to the compressive stress on the top side. The stress distribution is symmetrically distributed from the neutral axis of the bending specimen to the cell walls above and below and increases with increasing distance from the neutral axis. The cell walls below the loaded surface in the longitudinal direction of the component seem to be the best way to rigidify a component under bending load. Without the cell walls the stresses increase sharply in the remaining vertical walls as well as in the shell of the bending specimen. The cell walls aligned parallel to the loaded surface further reduce stresses in the specimen surface and can be combined with the positive effects of increased shell wall thickness [14].

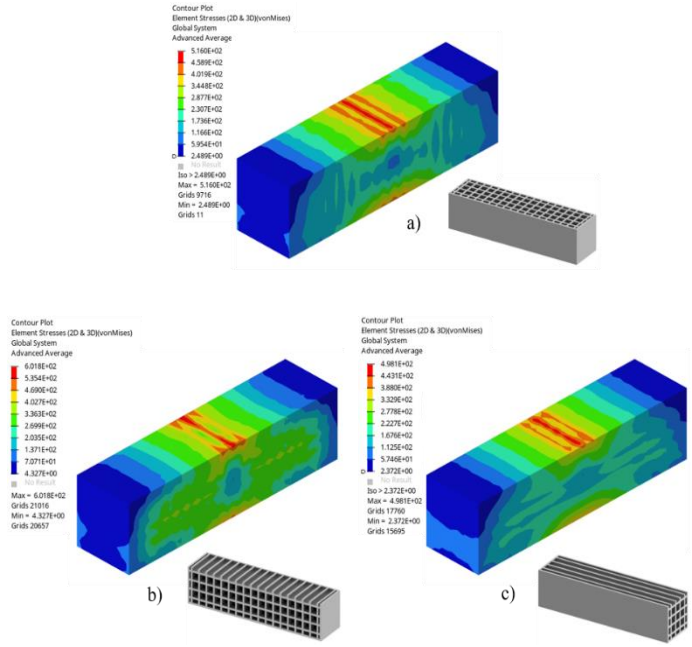

FIGURE 10: Stress distribution in the surface of a bending specimen with grid structure and infill degree of φ=60%, orientation of infill structure: α=0° and β=0° (a), α=90° and β=0° (b), α=0° and β=90° (c).

The diagram in Figure 11 displays the maximum stress as a function of different angles for a wall thickness of 1mm and load of 20kN for grid and honeycomb structures. For the grid structures, the maximum stress decreases steadily from 330MPa (15°) to 302MPa (90°) depending on the angle α. In contrast, the maximum stress for the honeycomb structures increases steadily from 336MPa (15°) to 347MPa (90°) as a function of the angle. Due to the wall orientations grid structures are to be favored for larger angles, as stress peaks could be reduced. For angles β 15° to 60°, the stresses vary between 357MPa and 387MPa for the grid structures and subsequently decrease to 340MPa with greater angle. In contrast, for the honeycomb structures, the stresses decrease from 354MPa (β = 15°) to 300MPa (β = 90°)

and are throughout smaller than for the grid structures at any angle. In the case of the grid structures, as γ is varied, the stresses increase with increasing angle from 411MPa (15°) to 464MPa (45°). A comparison with the honeycomb structures shows that the stresses vary in the range of 441MPa (γ = 30°) and 402MPa (γ = 45°) and tend to decrease at larger angles. The stresses are smaller for 30° and 45° than for the grid structures. A final consideration of the angles leads to the observation that the stresses are the lowest at an angle α for the grid structures. The variation of the angle β has a greater influence on the occurrence of stress peaks for grid and honeycomb structures, which can be better reduced with increasing angle for honeycomb structures. Nevertheless, the stresses are highest at the γ angle for both the grid and honeycomb structures. There seems to be a tendency to reduce the occurrence of stress peaks as the angle increases.

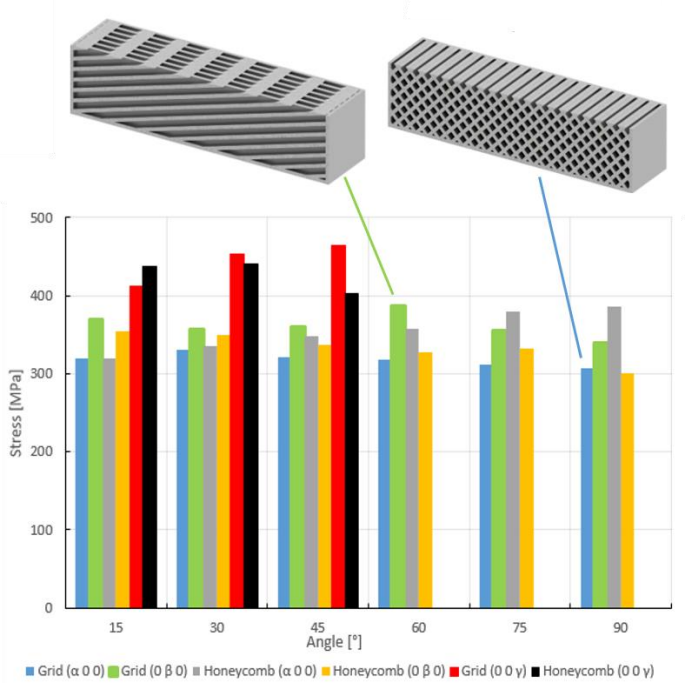

FIGURE 11: Maximum stresses depending on angle (α = 15° to 90°); (β = 15° to 90°); (γ = 15° to 45°) at 1mm wall thickness and load 20kN for grid and honeycomb infill (infill degree φ=60%).

The influence due to a changed cell wall thickness b_x is also investigated under bending load, the considered orientations of the infill structure are (α = 0°, β = 0°, γ = 0°) and can be compared within the test series on the influence of the infill degree at the identical orientations. The infill level of this simulation series is set to φ=60 % (see fig. 12). The maximum stress of the bending specimen frequently occurs in the load application. Increasing the wall thickness for grid structures can lead to a distribution of the stress levels towards the edge regions of the beam elements (fig. 12 a-c). In comparison, the maximum stress level is concentrated in the center of the bending beam, regardless of the wall thickness (fig. 12 d-g). Independent of the infill structure, the stress peaks occur in the areas of the voids of the infill with increasing wall thickness. Likewise, the maximum stress increases with increasing wall thickness for these constellations (see fig.12).

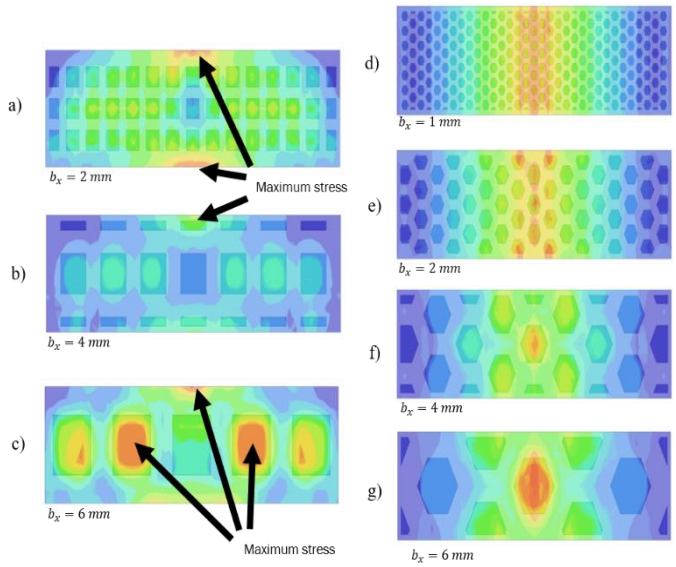

FIGURE 12: Representation of the stress distribution for different wall thicknesses b_x, grid (a-c, side view) and honeycomb (d-g, top view) infill structures.

Figure 13 displays the maximum stresses for the grid and honeycomb structures for different angles and wall thicknesses. It can be observed that the grid structure (α = 0°, β = 90°, γ = 0°) has the lowest stresses with a maximum of 420MPa (b_x =1mm). The wall thickness of 8mm has not been simulated, because the threshold of the stress was already exceeded at 6mm. It appears that the wall thickness has little effect on the stresses in this configuration. The highest stress occurs in the grid structures (α = 90°, β = 0°, γ = 0°) with a wall thickness of 4mm, since in this case there are the fewest walls along the force application and thus the stress is concentrated at 698MPa. Furthermore, it can be recognized an increase of the maximum stress for the honeycomb structures (α = 0°, β = 0°, γ = 0°) angle configuration with increasing wall thickness, due to the fact that the stress peaks concentrate in the voids (compare fig. 12). This finding can also be made for the other honeycomb configurations (α = 90°, β = 0°, γ = 0°) and (α = 0°, β = 90°, γ = 0°) up to a wall thickness of 4mm. At a wall thickness greater than 4mm, the stresses decrease due to the parametric design and less stress peaks appear in the voids. In general, the highest stresses occur at wall thicknesses of 4mm to 8mm, which is due to a smaller number of cells and thus stress peaks are concentrated on a few cells. In the case of high cell wall thicknesses additional cell walls must be inserted in the load application area to ensure uniform load transfer into the infill structure. An alignment of the cell walls along the beam is also advantageous here. Despite the coarser structure an increase in cell size can lead to a relief

of the entire component due to the fusion of cell walls and the shell.

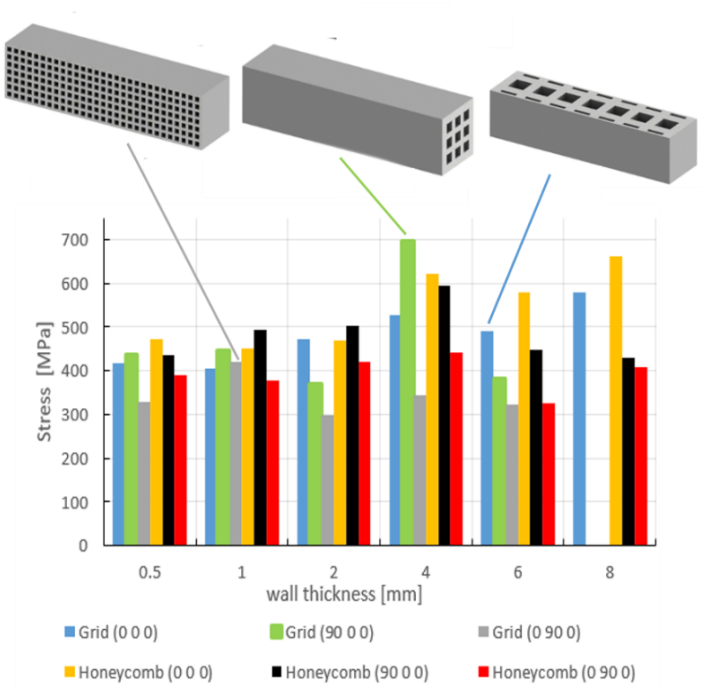

FIGURE 13: Representation of maximum stress for different wall thicknesses, orientations and infill structures (infill degree of φ=60%).

4. CONCLUSION

In this work grid and honeycomb structures were simulatively investigated with compression and bending simulations. It was shown that the parametric design was successfully developed for grid and honeycomb structures. By varying the cell wall thickness, the degree of infill and the orientations, holistic insights into the maximum stresses in the test geometries could be obtained. Both grid and honeycomb structures show superior behavior compared to each other for different configurations and load conditions. With the results one structure cannot be preferred, rather must be used application-dependent. Furthermore, it was found exactly that infill structures have a supporting share in the stresses that occur and 60% infill has comparable maximum stress levels to the solid material and thus a material saving of 40% can be realized for components with infill. With the findings gained from this paper, the production time for components can be significantly reduced where the load situation is estimable and thus component failure prevented. One possible application is for components where the outer structure cannot be changed and yet a material saving is to be achieved, such as in aerospace, automotive, spare parts or toolingmalking. The simulations will be modified for realistic use cases in the future.

Since this study was conducted in a purely simulative manner, it needs to be validated with experimental studies and will be presented in future work. Furthermore, different geometries should be investigated to capture the diversity of 3D-printed components. Likewise, dynamic load conditions in the infill can be supplemented by time-dependent simulations. The compression and 3-point bending tests have been performed to investigate the stresses in the part for the geometries according to the standards. The different configurations can of course be integrated into the other design features of the additively manufactured parts. The simulation results can be successfully applied to extend existing design guidelines and to enable an efficient initial accurate manufacturing. By specific adjustments of the material parameters, these results can be extended not only for the guidelines of the investigated material 316L [15], but also for other design guidelines with materials like IN718 [16] and Ti6Al4V [17]. This opens up new perspectives for the design of infill structures in the context of Design for Additive Manufacturing (DfAM). The ability to apply simulation results to different materials, taking into account specific properties, marks a significant advance in additive manufacturing technology. This enables optimized component manufacturing that simultaneously maximizes material utilization and meets mechanical performance requirements. The results obtained are thus instrumental in expanding the range of applications of DfAM and fully exploiting its potential, making a significant contribution to the development of advanced manufacturing methods.

ACKNOWLEDGEMENTS

The author declare no conflict of interests.

REFERENCES

[1] Sabban, R.; Bahl, S.; Chatterjee, K.; Suwas, S., Globularization using heat treatment in additively manufactured Ti-6Al-4V for high strength and toughness., Acta Mater. **2019**, 162, 239–254.

[2] Ge, J.; Lin, J.; Lei, Y.; Fu, H. Location-related thermal history, microstructure, and mechanical properties of arc additively manufactured 2Cr13 steel using cold metal transfer welding., Mater. Sci. Eng. A 2018, 715, 144–153.

[3] Qian Zhang, Wenwang Wu, Jainlin Liu; „Local Strengthening Design and Compressive Behavior Study of the Triangular Honeycomb Structure" Mdpi Metals 2022, 12(11), 1779; https://doi.org/10.3390/met12111779

[4] Liang-Yu Chen, Shun-Xing Liang, Yujing Liu, Lai-Chang Zhang, Additive manufacturing of metallic lattice structures: Unconstrained design, accurate fabrication, fascinated performances, and challenges, Materials Science and Engineering: R: Reports Volume 146, October 2021, 100648, https://doi.org/10.1016/j.mser.2021.100648

[5] Tomáš Goldmann, Wei-Chin Huang, Sylwia Rzepa, Jan Džugan, Radek Sedláče and Matej Daniel "Additive Manufacturing of Honeycomb Lattice Structure—From Theoretical Models to Polymer and Metal Products" Mdpi Materials 2022, 15(5), 1838; https://doi.org/10.3390/ma15051838

[6] D. Jin, D.J. Tian, J.H. Li and M. Sakane "Low-cycle fatigue of 316L stainless steel under proportional and nonproportional loadings", Fatigue & Fracture of

Engineering Materials & StructuresVolume 39, Issue 7Jul 2016 Pages 791-920
[7] Itthidet Thawon, Thongchai Fongsamootr, Yuttana Monaand Pana Suttaku, Investigation of the Mechanical Properties of Additively Manufactured Metal Parts with Different Relative Densities, Mdpi *Appl. Sci.* 2022, *12*(19), 9915; https://doi.org/10.3390/app12199915
[8] Maitane Gabilondo, Xabier Cearsolo, Mario Arrue and Francisco Castro, Influence of Build Orientation, Chamber Temperature and Infill Pattern on Mechanical Properties of 316L Parts Manufactured by Bound Metal Deposition, Mdpi Materials 2022, 15(3), 1183; https://doi.org/10.3390/ma15031183
[9] Yun Zhou a, Xiaoqing Zuo and Ting Zhang, 316L Stainless Honeycombs Fabricated by Extruding and Sintering, Advanced Materials Research Online: 2010-10-27 ISSN: 1662-8985, Vols. 146-147, pp 1921-1924 doi:10.4028/www.scientific.net/AMR.146-147.1921
[10] ASTM E9-09; Standard Test Methods of Compression Testing of Metallic Materials at Room Temperature, Last Updated: Jan 25, 2018; last access 30.04.23; https://www.astm.org/e0009-09.html
[11] ISO 7438:2020 Metallic materials — Bend test; last access 30.04.2023; https://www.iso.org/standard/72187.html
[12] Pernet, Benoît; Nagel, Jacquelyn Kay; Zhang, Hao; Compressive Strength Assessment of 3D Printing Infill Patterns; Procedia CIRP 105, 2022, 682-687; 10.1016/j.procir.2022.02.114
[13] Material Data Sheet EOS StainlessSteel 316L, https://www.fabb-it.de/files/datenblaetter/edelstahl.pdf, last access 30.04.2023
[14] Lubombo, C., & Huneault, M. (2018). Effect of Infill Patterns on the Mechanical Performance of Lightweight 3D-Printed Cellular PLA Parts. Materials Today Communications. doi:10.1016/j.mtcomm.2018.09.017
[15] Karim Asami et al. Design Guidelines For Green Parts Manufactured With Stainless Steel In The Filament Based Material Extrusion Process For Metals (MEX/M), European Powder Metallurgy Association, Ed., World PM2022 Proceedings, 2022.
[16] D. Herzog, K. Asami, "Design guidelines for laser powder bed fusion in Inconel 718," *Journal of Laser Applications*, vol. 34, no. 1, p. 12015, 2022, doi: 10.2351/7.0000508.
[17] K. Asami, K. Bartsch, and C. Emmelmann, "Design-Richtlinie für die ressourceneffiziente Gestaltung von Stützstrukturanbindungen im pulverbettbasierten Laserstrahlschmelzen von Ti6Al4V: Design rule for efficient support connection point spacing in laser powder bed fusion of Ti6Al4V," in *Proceedings of the 17th Rapid.Tech 3D Conference Erfurt, Germany, 22–23 June 2021*, M. Kynast, G. Witt, and M. Eichmann, Eds., München: Carl Hanser Verlag GmbH & Co. KG, 2021, pp. 80–88.